The Journal of Chemical Physics ARTICLE scitation.org/journal/jcp

Curvature and temperature-dependent thermal interface conductance between nanoscale gold and water

Cite as: J. Chem. Phys. 157, 054703 (2022); doi: 10.1063/5.0090683
Submitted: 8 March 2022 • Accepted: 27 June 2022 •
Published Online: 4 August 2022

Blake A. Wilson,[1] Steven O. Nielsen,[2] Jaona H. Randrianalisoa,[3] and Zhenpeng Qin[1,4,5,6,a)]

AFFILIATIONS

[1] Department of Mechanical Engineering, The University of Texas at Dallas, Richardson, Texas 75080, USA
[2] Department of Chemistry and Biochemistry, The University of Texas at Dallas, Richardson, Texas 75080, USA
[3] Institut de Thermique, Mécanique, Matériaux, Université de Reims Champagne-Ardenne, Reims, France
[4] Department of Bioengineering, The University of Texas at Dallas, Richardson, Texas 75080, USA
[5] The Center for Advanced Pain Studies, The University of Texas at Dallas, Richardson, Texas 75080, USA
[6] Department of Surgery, The University of Texas at Southwestern Medical Center, Dallas, Texas 75390, USA

[a)] **Author to whom correspondence should be addressed:** zhenpeng.qin@utdallas.edu

ABSTRACT

Plasmonic gold nanoparticles (AuNPs) can convert laser irradiation into thermal energy for a variety of applications. Although heat transfer through the AuNP–water interface is considered an essential part of the plasmonic heating process, there is a lack of mechanistic understanding of how interface curvature and the heating itself impact interfacial heat transfer. Here, we report atomistic molecular dynamics simulations that investigate heat transfer through nanoscale gold–water interfaces. We simulated four nanoscale gold structures under various applied heat flux values to evaluate how gold–water interface curvature and temperature affect the interfacial heat transfer. We also considered a case in which we artificially reduced wetting at the gold surfaces by tuning the gold–water interactions to determine if such a perturbation alters the curvature and temperature dependence of the gold–water interfacial heat transfer. We first confirmed that interfacial heat transfer is particularly important for small particles (diameter ≤10 nm). We found that the thermal interface conductance increases linearly with interface curvature regardless of the gold wettability, while it increases nonlinearly with the applied heat flux under normal wetting and remains constant under reduced wetting. Our analysis suggests the curvature dependence of the interface conductance coincides with changes in interfacial water adsorption, while the temperature dependence may arise from temperature-induced shifts in the distribution of water vibrational states. Our study advances the current understanding of interface thermal conductance for a broad range of applications.

I. INTRODUCTION

Plasmonic nanoparticles can absorb and convert light into heat due to a photothermal process known as plasmonic heating.[1] In particular, gold nanoparticles (AuNPs) are commonly used as plasmonic nanoheaters in a wide range of applications, including hyperthermia-based tumor ablation,[2–5] selective protein inactivation,[6–10] nanobubble theranostics,[11] nanothermometry,[12,13] photothermal imaging,[14,15] and photoacoustic imaging.[16,17] Interfacial heat transfer is particularly relevant for nanoscale heat transfer because individual nanostructures exhibit a high surface-to-volume ratio and their ensembles have a high density of interfaces.[18,19] As such, heat transfer through the interface between an AuNP and its surrounding medium is an important element of the plasmonic heat dissipation process.[20,21] A thorough understanding of AuNP thermal interface conductance can be critical for precise control of plasmonic heat dissipation and its applications.[11,16]

Interfacial heat transfer can be characterized by the thermal interface conductance (G), which quantifies the rate at which heat flows through an interface between two adjacent media at different temperatures. Experimental studies indicate that the thermal interface conductance of nanoparticles is affected by the chemical

composition of the nanoparticle, its ligand coating, and the surrounding medium.[20,22–26] Molecular dynamics simulation studies of solid nanospheres immersed in monatomic fluids and nanodroplets of n-decane in water suggest that interface curvature (inversely proportional to particle size) and temperature can also affect nanoparticle thermal interface conductance.[27–29] Recent molecular dynamics studies also report that AuNPs immersed in organic solvent exhibit curvature-dependent changes in thermal interface conductance.[30,31] Although previous experiments indicate that characteristic times for AuNP cooling in water scale with particle surface area,[32] it remains unclear if interface curvature or temperature affects the thermal conductance at nanoscale gold–water interfaces. These factors are of practical importance in biomedical applications that utilize plasmonic heating of AuNPs because the AuNPs are embedded in primarily aqueous media and may experience significant temperature variations.

In this article, we use atomistic molecular dynamics simulations to investigate the effects of temperature and curvature on heat transfer through bare nanoscale gold interfaces with water during continuous plasmonic heating. We simulated four nanoscale gold surfaces with different curvatures under two wetting conditions (normal vs reduced), and subjected each gold structure to various heating intensities to account for the effects of temperature increases during plasmonic heating. Altering the gold wettability allowed us to account for how differences in the gold–water interaction potential could affect the heat transfer and computationally determine if the observed trends are robust to such changes. First, we confirmed that our results for the interface thermal conductance fall within the range of values reported from experiments and that the thermal interface conductance plays a critical role in AuNP heat dissipation, particularly, for small AuNPs (≤10 nm in diameter). Next, we found that the thermal interface conductance increases with curvature under both wetting conditions, but it increases nonlinearly with heat flux only under normal wetting of the gold surface. Our analysis reveals that the curvature dependence of the interface conductance is due to the changes in interfacial water adsorption, while the temperature dependence is caused by heat-induced shifts in the distribution of water vibrational states. This work advances our understanding of how temperature and curvature affect the thermal conductance across nanoscale gold–water interfaces.

II. METHODS

A. Model system construction

In order to evaluate the impact of interface curvature on the heat transfer between nanoscale gold and water, we modeled in atomistic detail four nanoscale gold–water interfaces of different curvatures [Fig. 1(a)]: three spherical AuNPs with diameters (d) of 3, 5, and 10 nm and a planar gold–water interface to represent the zero-curvature limit. The nanoscale gold structures were constructed and immersed in water using the Visual Molecular Dynamics (VMD) software.[33] The planar gold slab was constructed as a rectangular block of Au_{111} with dimensions of

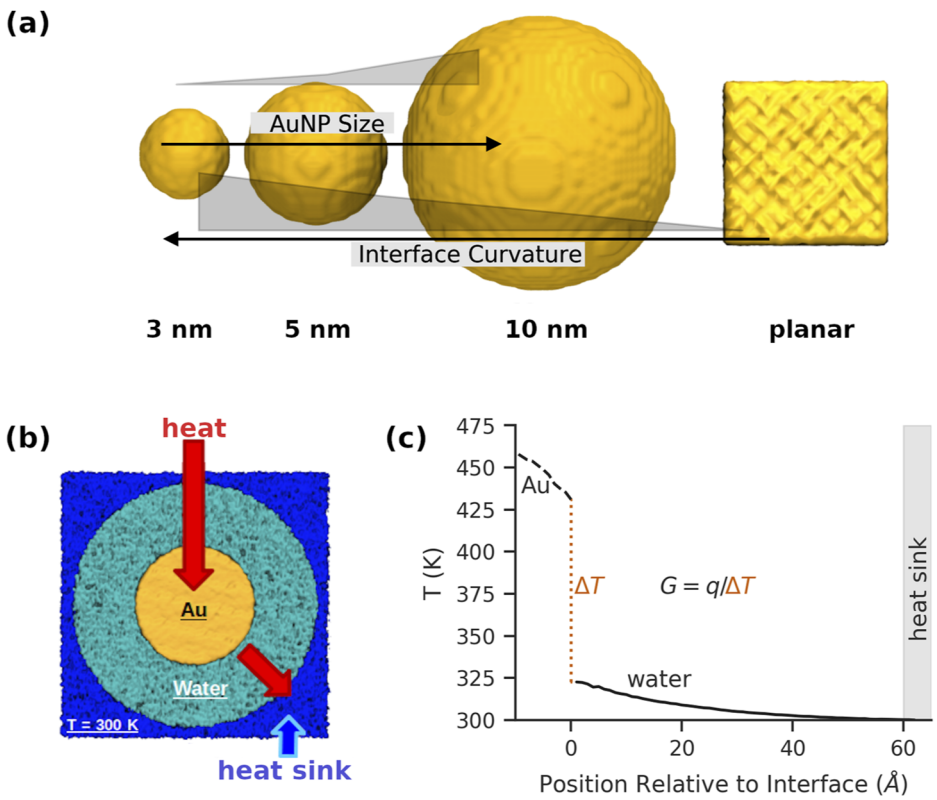

FIG. 1. Simulation design. (a) Images depicting the simulated gold surfaces. (b) Simulation design for the spherical AuNP geometry. Heat is applied uniformly to the gold atoms while the dark blue region of water acts as a heat sink, maintained at T = 300 K. (c) Representative temperature profile for a AuNP under continuous heating, which demonstrates the temperature jump at the interface.

69.4 × 69.4 × 70.4 Å^3 (20 230 gold atoms), and the two faces along the z-dimension were solvated with layers of water with thickness 190.7 Å (185 919 total water atoms including both layers). Overall, the planar gold–water system consisted of a total of 206 149 atoms with box dimensions of 69.4 × 69.4 × 450.8 Å^3 with the gold slab centered at the origin. Each spherical AuNP was constructed by extracting a spherical selection of atoms within the AuNP's specified diameter from a large block of Au_{111}. The AuNPs consisted of 887, 3925, and 30 885 gold atoms for the 3, 5, and 10 nm AuNPs, respectively. The AuNPs were then solvated with cubic boxes of water containing 88 317, 187 459, and 378 583 water molecules with side lengths of 140.00, 180.00, and 230.00 Å for the 3, 5, and 10 nm AuNPs, respectively. In all AuNP systems, the AuNP was centered at the origin.

B. Molecular dynamics simulations

All molecular dynamics simulations were carried out with the Large-scale Atomic/Molecular Massively Parallel Simulator (LAMMPS) software (http://lammps.sandia.gov).[34] Periodic boundary conditions were used in all cases. Note that under periodic boundary conditions, the planar gold slab extends semi-infinitely in the xy plane.

Gold–gold interactions were modeled using the embedded atom model,[35] which is a many-body potential that more accurately represents metallic bonding than standard pairwise potentials. Water was modeled using the fully flexible simple point charge extended (SPCE-F) model,[36] chosen primarily for its ability to reasonably estimate the experimental surface tension of water at temperatures between 300 and 500 K. With the SPCE-F model, the van der Waals interactions are described by a standard 12-6 Lennard-Jones potential, defined as

$$U_{ij} = 4\varepsilon_{ij}\left[\left(\frac{\sigma_{ij}}{r}\right)^{12} - \left(\frac{\sigma_{ij}}{r}\right)^{6}\right], \quad r < r_c, \tag{1}$$

for atoms i and j separated by distance r, with a cutoff distance of r_c. ε_{ij} is the energy coefficient (kJ mol^{-1}) describing the strength of the interaction, and σ_{ij} (Å) is the zero-energy distance describing the sizes of interacting atoms. Only the water O–O interactions are nonzero with ε_{O-O} = 0.65 kJ mol^{-1} and σ_{O-O} = 3.1661 Å. The intramolecular H–O bond stretching is modeled with a harmonic potential given by

$$U_{bond} = K_b(b - b_0)^2, \tag{2}$$

for bond distance b with force constant K_b = 2322.20 kJ mol^{-1} Å^{-2} and equilibrium bond distance b_0 = 1.0 Å. The intramolecular H–O–H angle is also maintained with a harmonic potential

$$U_{angle} = K_a(\theta - \theta_0)^2, \tag{3}$$

for angle θ with force constant K_a = 191.7549 kJ mol^{-1} rad^{-2} and equilibrium angle θ_0 = 109.4°.

The interaction between gold and water was also modeled using a standard 12-6 Lennard-Jones potential. Only the oxygen–gold interactions were included in the description of the gold–water interaction. The parameters for the water oxygen and gold interactions were ε_{O-Au} = 2.47 kJ mol^{-1} and σ_{O-Au} = 3.6 Å as developed by Merabia *et al.* to reproduce a wetting condition with a gold–water contact angle <30°.[37] However, there are other models and parameterizations for the gold–water interaction available in the literature,[38–41] which may affect wetting at the interface and, thus, yield different interfacial heat transfer between gold and water.[42] Additionally, the standard 12-6 Lennard-Jones potential [Eq. (1)] does not explicitly include image charge effects arising from the polarization of the metal atoms at the interface,[43,44] which also influences adsorption at the metal surface and may alter the simulated interfacial heat transfer.[45] To determine whether altering the gold-water interactions affects the curvature and temperature dependence of the thermal interface conductance, another series of simulations were carried out in which the Lennard-Jones interaction between gold and water was adjusted to ε_{O-Au} = 0.59 kJ mol^{-1} and σ_{O-Au} = 3.383 Å. Since the wetting and interfacial heat transfer are also strongly affected by the strength of interactions between the solid and liquid atoms,[27,46] this significant weakening of the interaction between gold and water is expected to reduce wetting at the interface and the rate of interfacial heat transfer. We, thus, denote this case as the *reduced wetting* case, and the simulations using the unaltered interaction parameters from Merabia *et al.* are denoted as the *normal wetting* case.[37] All model parameters are summarized in Table S4 (supplementary material).

A global cutoff of r_c = 10 Å was used for the Lennard-Jones interactions. The particle–particle particle-mesh solver was used for electrostatics with a desired relative error in the forces of 0.0001 and a switching cutoff of 8 Å for smoothly transitioning to long range electrostatics.[47] The gold structures were prevented from drifting during the simulations by tethering their center of mass to the origin using a harmonic spring with force constant 960 kJ mol^{-2} Å^{-1}.

Initially, each nanoscale gold–water system was energy minimized using a conjugate gradient algorithm. The systems were then equilibrated under canoncial ensemble (NVT) conditions for 1 ns at 300 K with a Nosé–Hoover thermostat. A second equilibration phase followed this under isothermal-isobaric (NPT) conditions for 1 ns at 300 K and 1 atm using a Nosé–Hoover thermostat and Nosé–Hoover barostat with isotropic coupling of the simulation dimensions. A time step of 1 fs was used to integrate the equations of motion. A separate set of simulations were carried out following a similar procedure to generate equilibrated versions of each system at 370 K and 1 atm.

Heat transfer between the nanoscale gold and water was modeled using a nonequilibrium steady-state approach like that employed by Merabia *et al.* and Chen *et al.*,[37,42] which approximates plasmonic heating of the gold under continuous-wave laser stimulation. The nonequilibrium simulations were initialized from previously equilibrated configurations at 300 K and 1 atm in each case. The gold structure was then subjected to continuous heating at a given heat power Q using a heat exchange algorithm that adds non-translational kinetic energy to the gold atoms. A Langevin thermostat K was applied to water molecules in the outermost portion of the simulation cell to maintain the temperature in that region at 300 K [Fig. 1(b)],[48] providing a heat sink for heat added to the gold structure while allowing the temperature of water to increase locally in the vicinity of the gold surface. In the planar gold–water system, the heat sink was defined as the region encompassing $z > 200$ Å and $z < -200$ Å within the unit cell; note that these two regions are joined into a single region by the periodic boundary conditions. In the AuNP systems, the heat sink region was defined using a radial distance criterion, namely, the region encompassing $r > 65$ Å,

$r > 85$ Å, and $r > 110$ Å from the origin, for the 3, 5, and 10 nm AuNPs, respectively. The equations of motion were integrated under isoenthalpic-isobaric (NPH) conditions with a pressure of 1 atm using a Nosé–Hoover barostat with isotropic coupling of the simulation dimensions and a time step of 1 fs. This simulation design yields an initial transient phase during which the gold temperature increases in response to the applied heat before reaching a stable steady state (Figs. S1 and S2, supplementary material). Note, however, that the enthalpy (H) of the system is not conserved during the transient phase and can increase before reaching a stable steady state [Fig. S3(a), supplementary material], despite the isoenthalpic integration applied to the equations of motion. There may also be a corresponding thermal expansion of the system volume during the transient phase [Fig. S3(b), supplementary material]. The nonequilibrium steady-state simulations were run for 2, 3, 4, and 6 ns for the 3, 5, and 10 nm AuNPs and planar slab, respectively. For the reduced wetting case, the simulation times were all 4 ns.

An additional set of simulations was performed to estimate the velocity autocorrelation functions of gold and water at temperatures of 300 K and 370 K. These simulations were initialized from the previously equilibrated configurations at 300 or 370 K and 1 atm and were executed with a time step of 0.25 fs under microcanoncial ensemble (NVE) conditions. In each case, simulations were run for a total of 40 000 time steps, and the velocity autocorrelation function was computed for two time origins taken over two consecutive 20 000 time step intervals.

C. Analysis

Simulation analysis was carried out using a combination of LAMMPS functionality, Python code (https://www.python.org), and VMD scripts (https://www.ks.uiuc.edu/Research/vmd).[33] Our analysis in Python incorporated various libraries, including MDanalysis,[49,50] SciPy,[51] NumPy,[52] Matplotlib,[53] seaborn,[54] Numba,[55] pandas,[56] and Jupyter.[57] Simulation snapshots were rendered from VMD using the Tachyon ray tracer.[58]

In the analysis of the nonequilibrium steady-state simulations, we discarded the first 1 ns of the AuNP system trajectories and the first 3 ns of the planar slab system. In the reduced wetting case, we adjusted the time to 2 ns for the 5 and 10 nm AuNP systems. We visually inspected the time course of the gold temperature (Figs. S1 and S2, supplementary material) and simulation box volume [Fig. S3(b), supplementary material] to confirm that the systems were no longer in the transient phase and had reached a steady state by those times.

III. RESULTS AND DISCUSSION

A. Analysis of the thermal interface conductance

The thermal interface conductance (G) was used to quantify heat transfer through the gold–water interface during the steady-state phase of the nonequilibrium molecular dynamics simulations. In the nonequilibrium simulations, the gold structure is subjected to continuous heating at a specified heat power while an outer region of water is maintained at 300 K [Fig. 1(b)], approximating plasmonic heating of gold under continuous-wave laser stimulation.[37,42] Under these conditions, the steady-state temperature profile in the direction normal to the interface between gold and water exhibits a temperature jump (ΔT) [Fig. 1(c)], which is inversely proportional to G,

$$G = \frac{Q}{A\Delta T} = \frac{q}{\Delta T}, \tag{4}$$

where $q = Q/A$ is the heat flux across the interfacial area A, which is taken as the gold surface area: $A = \pi d^2$ for spherical AuNPs with diameter d and $A = 2L_xL_y$ for the planar gold surface. L_x and L_y are the lateral dimensions of the gold surface within the simulation cell, and the factor of two accounts for the fact that two sides of the planar surface are exposed to solvent. In each case, instantaneous spatial temperature profiles for gold and water were computed separately with a spatial binning of width ~1 Å (radial shells for AuNPs and rectangular blocks along the z-direction for the planar slab) every 1 ps. Subsequently, bins with <100 atoms at any time point were dropped from the profile to reduce errors in the temperature estimation. The steady-state temperature profiles were then estimated by time averaging the instantaneous profiles within the designated steady-state portions of each trajectory (Figs. S4 and S5, supplementary material). The average values and standard errors of the thermal interface conductance G values were then estimated by block averaging the instantaneous temperature profiles.[59] For each block, ΔT was estimated as the temperature difference between the outermost gold spatial bin and the innermost water spatial bin. To account for the possibility of thermal expansion of the gold, the gold size (diameter for AuNPs and thickness for planar slab) was estimated from the outermost gold spatial bin position (Table S2, supplementary material). The corresponding G for the block was estimated according to Eq. (4). Block sizes of 200, 250, 500, and 750 ps were used for the block averages for the 3, 5, and 10 nm AuNPs and planar slab, respectively. In the reduced wetting case, the block sizes were adjusted to 200, 250, 400, and 300 ps for the 3, 5, and 10 nm AuNPs and planar slab, respectively. The gold temperature was examined using blocked standard error analysis with varying block sizes to confirm that these block sizes resulted in uncorrelated data for block averaging (Figs. S6 and S7, supplementary material). The reported error in G values was taken as 1.96 times the standard error estimate (from block averaging) and thus represents an estimate of the 95% confidence interval.

G ranged from ~110 to 185 MW m^{-2} K^{-1} for the normal wetting case, which falls within the range of experimental results (~100 – 250 MW m^{-2} K^{-1}) reported previously for spherical AuNPs in water (Fig. 2).[21,22,26] It should be noted, however, that the nanoparticles are passivated with molecules such as citrate in the experimental studies. When nanoparticles are coated with a layer of ligand molecules or other materials, the interfacial heat transfer is more complicated and consists of contributions from the gold–coating interface, coating–water interface, and the coating layer itself.[30,60] Therefore, the interface conductance from experiments necessarily represents an effective value incorporating those different contributions, whereas the simulated values from this study only include the gold–water interface. As expected, the artificial reduction of gold wetting in the reduced wetting case led to much lower G values, which ranged from ~20 – 45 MW m^{-2} K^{-1}. G of the planar surface in the normal wetting case was ~110 MW m^{-2} K^{-1} at all heating powers, which is close to the previously reported values of 105 ± 15 MW m^{-2} K^{-1} for 100 nm and 110 ± 10 MW m^{-2} K^{-1} for 18.5 ± 3.0 nm citrate-stabilized AuNPs in water.[21,26] The planar

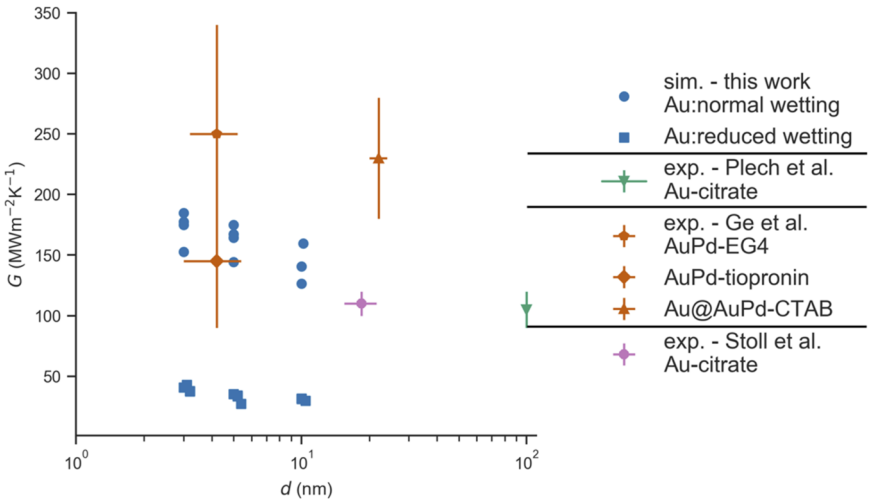

FIG. 2. Validation and comparison of thermal interface conductance calculations with experiments. The simulated nanoscale gold–water thermal interface conductance values (this study) are plotted vs particle diameter, along with experimental data for spherical nanoparticles in water. Note that the different values of G shown for the simulated AuNPs at a given size correspond to simulations at the various heating powers. Experimental data were collected from Plech *et al.*,[21] Ge *et al.*,[22] and Stoll *et al.*[26] Error bars were included for both G and d of the experimental data points if specified in the given references. EG4 = monohydroxy(1-mercaptoundec-11-yl)tetra-ethylene glycol; CTAB = cetyltrimethylammonium bromide.EG4 = monohydroxy(1-mercaptoundec-11-yl)tetra-ethylene glycol; CTAB = cetyltrimethylammonium bromide.

surface had a $G \sim 25$–26 MW m^{-2} K^{-1} in the reduced wetting case.

Recently, Jiang *et al.* reported an atomistic nodal approach to estimate thermal interface conductance across nanostructure surfaces with atomistic resolution.[61] They found that the conductance is heterogeneous across the nanostructure surface due to local differences in the surface structure and surface atom coordination for various nanostructure morphologies, including spherical particles. Therefore, it is worth noting that our estimates of G represent the composite averages over the whole surface of the gold structures.

1. Importance of thermal interface conductance for nanoparticles

For spherical AuNPs, the relative importance of G in regulating their heat dissipation can be gauged by the Kapitza number,[1]

$$\lambda_K = \frac{2l_K}{d} = \frac{2\kappa_W}{Gd}, \tag{5}$$

where l_K is the Kapitza length,[62,63] d is the particle diameter, and κ_W is the thermal conductivity of the surrounding water. If $\lambda_K \ll 1$, the heat transport is limited by heat diffusion through water and interfacial heat transfer has little effect on the process. In contrast, if $\lambda_K \gg 1$, the heat transport is limited by the interface. By setting $\lambda_K = 1$, we can define a critical G value,

$$G_c = \frac{2\kappa_W}{d}. \tag{6}$$

Analogously, when $G \gg G_c$, AuNP heat dissipation is limited by heat diffusion through water, and when $G \ll G_c$, it is limited by the interface. Heat transfer through the interface only has a negligible impact on the kinetics of AuNP heat dissipation in the former case (i.e., when $G \gg G_c$). To gauge the relative importance of heat transfer through the gold–water interface to AuNP heat dissipation, we compared the G values from our simulated cases as well as those reported from experiments of AuNPs in water with G_c evaluated across a range of AuNP sizes (Fig. 3). When calculating G_c, we used a constant $\kappa_W = 0.6$ W m^{-1} K^{-1}, which is consistent with experimentally measured κ_W values around 300 K.[64] In comparison, we estimate the thermal conductivity for the flexible water model used in our simulations is $\kappa_W \sim 1.2$ W m^{-1} K^{-1} (Fig. S8, supplementary material), which is about a factor of 2 higher than the experimental value used to estimate G_c. From this analysis, we confirm that for AuNPs within the size range we have simulated ($d \leq 10$ nm), interfacial heat transport is a particularly important factor in their heat dissipation, with $G \lesssim G_c$ under both wetting conditions when considering $\kappa_W = 0.6$ W m^{-1} K^{-1}. This is also the case when considering the elevated thermal conductivity of the water model since the corresponding G_c would be about a factor 2 higher than that shown in Fig. 3. For the simulated reduced wetting case, the G values of the 3 and 5 nm AuNPs even approach the boundary for interface limited heat dissipation. Considering the experimental estimates of G for AuNPs in water,[21,22,26] it appears that G only approaches the boundary for thermal diffusion limited heat dissipation around $d \sim 100$ nm, suggesting that the interface slows AuNP heat dissipation for diameters $d < 100$ nm. However, coating AuNPs with a sufficiently hydrophilic ligand such as polyethylene glycol (PEG) may lead to much higher G,[25] which may make heat dissipation out of particles with $d < 100$ nm thermal diffusion limited. Conversely, G for CTAB-stabilized gold nanorods in water may be as low as ~50 MW m^{-2} K^{-1} in some cases,[65] so more hydrophobic ligands will promote interface limited heat dissipation out of AuNPs with $d \leq 5$ nm.

2. Temperature dependence of thermal interface conductance

For the normal wetting case, G of the spherical AuNPs exhibited a nonlinear dependence on the heat flux [Fig. 4(a)], increasing

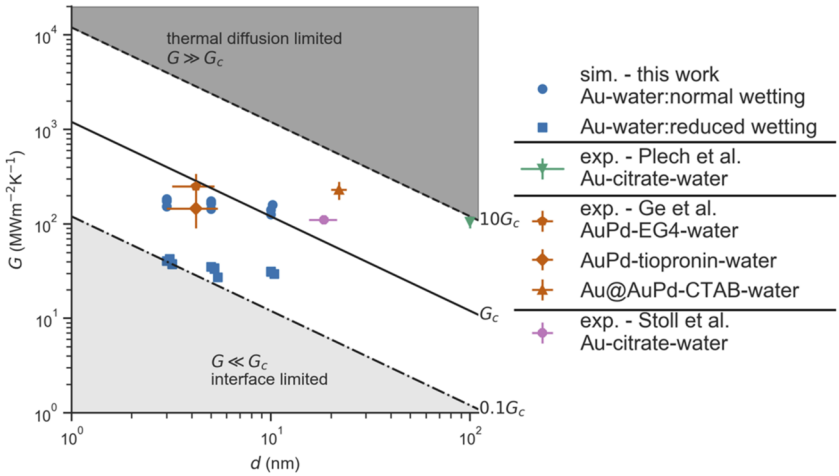

FIG. 3. Analysis of critical thermal interface conductance reveals importance of interface conductance for small nanoparticles ($d \leq 10$ nm). The simulated nanoscale gold–water thermal interface conductance values (this study) are plotted vs particle diameter and compared to the critical value of the thermal interface conductance G_c (solid line), along with experimental data for spherical AuNPs in water. Experimental data were collected from Plech *et al.*,[21] Ge *et al.*,[22] and Stoll *et al.*[26] The boundaries between the thermal diffusion limited regime (dark gray region) and the interface limited regime (light gray region) were taken as $G = 10G_c \gg G_c$ (dashed line) and $G = 0.1G_c \ll G_c$ (dashed-dotted line), respectively. A constant $\kappa_W = 0.6$ W m^{-1} K^{-1} was used when computing G_c values. EG4 = monohydroxy(1-mercaptoundec-11-yl)tetra-ethylene glycol; CTAB = cetyltrimethylammonium bromide.

by about 20%–40% from the lowest to the highest heating intensities for the spherical AuNPs. Since the applied heating power affects the temperature of both the gold structure and surrounding water (Fig. S9, supplementary material), an increase in the thermal interface conductance with heat flux suggests an underlying temperature dependence. However, in the reduced wetting case, G did not exhibit a clear dependence on the heat flux [Fig. 4(b)], suggesting that wetting also plays a role in how G is affected by temperature.

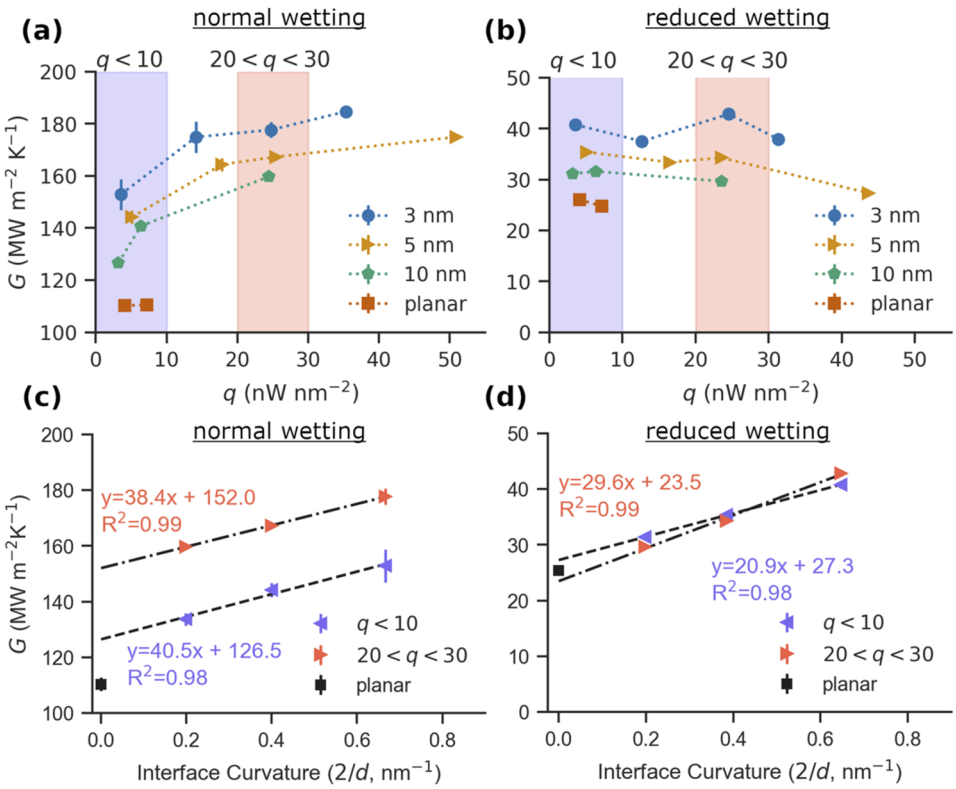

FIG. 4. Temperature dependence of thermal interface conductance. (a) Thermal interface conductance vs heat flux for the different gold–water interfaces in the normal wetting case. (b) Thermal interface conductance vs heat flux for the different gold–water interfaces in the reduced wetting case. (c) Interface conductance vs interface curvature under different levels of heating for the normal wetting case. (d) Interface conductance vs heat flux for different gold–water interfaces for the reduced wetting case. The dashed and dashed-dotted lines in (c) and (d) are the linear-fit lines consistent with Eq. (7): y (MW m^{-2} K^{-1}) corresponds to $G(d)$, x (nm^{-1}) corresponds to $2/d$, the slope ($\times 1000^{-1}$ MW m^{-1} K^{-1}) corresponds to δ, and the y-intercept (MW m^{-2} K^{-1}) is G_0.

Temperature-dependent thermal conductance has been observed in other systems. A linear dependence on temperature has been observed for thermal conductance at solid–solid interfaces at high temperature, which was attributed to an increase in inelastic scattering of phonons at the interface.[66,67] Various simulation studies have reported that the thermal interface conductance of nanoscale solid–fluid interfaces tends to increase with temperature,[68–70] typically following a power law expression. However, others indicate a decrease in the thermal interface conductance with temperature.[28,37,71,72] Chen *et al.* reported a dependence of the thermal interface conductance on heat intensity for simulations of a 3 nm spherical AuNP immersed in a flexible water model that was similar to the one we observed for the AuNPs,[42] but they also found that the thermal interface conductance was higher overall and did not change with heating power with a rigid water model.[42]

3. Curvature dependence of thermal interface conductance

Under both wetting conditions, the relative values of G are in order of planar <10 nm AuNP <5 nm AuNP <3 nm AuNP [Figs. 4(a) and 4(b)], suggesting a dependence on the interface curvature. Tascini *et al.* reported that the thermal interface conductance of solid nanospheres immersed in a monatomic fluid increased linearly with interface curvature according to the following expression:[27]

$$G(d) = \delta\frac{2}{d} + G_0, \tag{7}$$

where d is the particle diameter and $2/d$ the interface curvature, δ is the change in interface conductance with curvature, and G_0 is the interface conductance at the zero-curvature limit (i.e., $\lim_{2/d\to 0}$), which should match the conductance of the corresponding planar surface. Similarly, we found that at low and high heat fluxes, the thermal interface conductance of the spherical AuNPs increased linearly with the interface curvature in each heating regime as per Eq. (7) [Figs. 4(c) and 4(d)]; note that for both wetting conditions, we averaged the two G values for the 10 nm AuNP in the low heat flux regime for the linear fit. For the normal wetting case, the δ values were similar in both heating regimes (~0.04 W m^{-1} K^{-1}), and were consistent with values reported by Tascini *et al.* for nanoparticles with full wetting (δ ~ 0.023–0.105 W m^{-1} K^{-1}).[27] However, the corresponding values of G_0 were different due to the increase in G with heat flux. G_0 for the fit to the AuNP data in the low heat flux regime (126.5 MW m^{-2} K^{-1}) was also higher than the thermal interface conductance of the planar gold interface (~110 MW m^{-2} K^{-1}) in that heat flux regime. However, given that the heat fluxes are not exactly the same across the interfaces and that we averaged the two G values for the 10 nm AuNP in the low heat flux regime, as well as the limited number of AuNP sizes available for the linear fit, some error in the estimate of G_0 is to be expected. In the reduced wetting case, the δ values in the two heating regimes (~0.021 and ~0.03 W m^{-1} K^{-1}) were lower than in the normal wetting case, consistent with values reported by Tascini *et al.* for nanoparticles with partial (δ ~ 0.012–0.023 W m^{-1} K^{-1}) and full wetting (δ ~ 0.023–0.105 W m^{-1} K^{-1}).[27] In this case, the planar surface G values ~25 – 26 MW m^{-2} K^{-1} fall with the range of the G_0 estimates (27.3 and 23.5 MW m^{-2} K^{-1} for low and high heat fluxes, respectively).

Curvature dependence of the interface thermal conductance has previously been reported from simulations of other systems including solid nanospheres in monatomic Lennard-Jones fluids,[27,28,61] and nanodroplets of n-decane in water,[29] as well as solid and liquid ZnO nanoparticles in tetradecane.[73] In those cases, as with our simulations of the gold–water interface, $\delta > 0$ and the interface conductance increased with curvature (decreases with particle size) (Table S3, supplementary material). In contrast, G from simulations of bare spherical AuNPs in hexane exhibited the opposite trend with $\delta < 0$ (G decreases with curvature).[30,31] In this case, the curvature dependence was attributed to size-dependent changes in the structure, coordination, and vibrational modes of the AuNP surface atoms. In the case of n-decane nanodroplets, the increase in G with curvature (i.e., $\delta > 0$) was attributed to a reduction in the nanodroplet–water interface tension,[29] while in the case of solid nanospheres in monatomic fluid, Tascini *et al.* found that $\delta > 0$ corresponded to curvature-dependent differences in solvent adsorption density at the nanoparticle surfaces.[27] Jiang *et al.* have also recently reported a similar trend for G with the curvature of spherical nanoparticles that coincided with increased surface adsorption density.[61] Jiang *et al.* considered the role of surface atom coordination and found that G generally tends to decrease with the coordination number of the surface atoms and the coordination number of surface atoms increases with nanoparticle size. The coordination of surface atoms affects their solvent accessibility and their vibrational modes.[31] As such, it is another factor contributing to the interface conductance's curvature dependence.

B. Analysis of water adsorption at the nanoscale gold surfaces

The structuring and adsorption of solvent at a solid surface are important factors influencing the interfacial heat transfer and can have a large effect on thermal interface conductance.[46,74,75] For solid spherical nanoparticles, Tascini *et al.* found that smaller nanoparticles with larger curvature had higher surface adsorption density,[27] which coincided with the increases in G that they observed with the particle curvature. This result was also recently confirmed by Jiang *et al.* in their analysis of heterogeneous heat transfer at nanoparticle–liquid interfaces.[61] To determine if curvature-dependent changes in solvent adsorption could help explain the curvature dependence of the AuNP–water G, we examined the structuring and adsorption of water at the surfaces of nanoscale gold [Fig. 5(a)]. To characterize the water structuring and adsorption at the gold surfaces, we computed the mass density profiles of gold and water and quantified the surface adsorption density.[27] Instantaneous (spatial) mass density profiles for gold and water were computed separately with a spatial binning of width 0.25 Å (radial shells for AuNPs and rectangular blocks along the z-direction for the planar surface). At each time step, the coordinates of atoms were shifted so that the center of mass of the gold structure was at the origin. In the case of the planar surface, the profile was averaged over the positive and negative z-directions. The profiles for systems in the absence of heating were computed by averaging over the final 500 ps of the equilibration simulations, which were under NPT conditions at 300 K and 1 atm. For systems under heating, the steady-state profile was computed by time averaging the instantaneous profiles over the final 1 ns of each nonequilibrium steady-state simulation. The

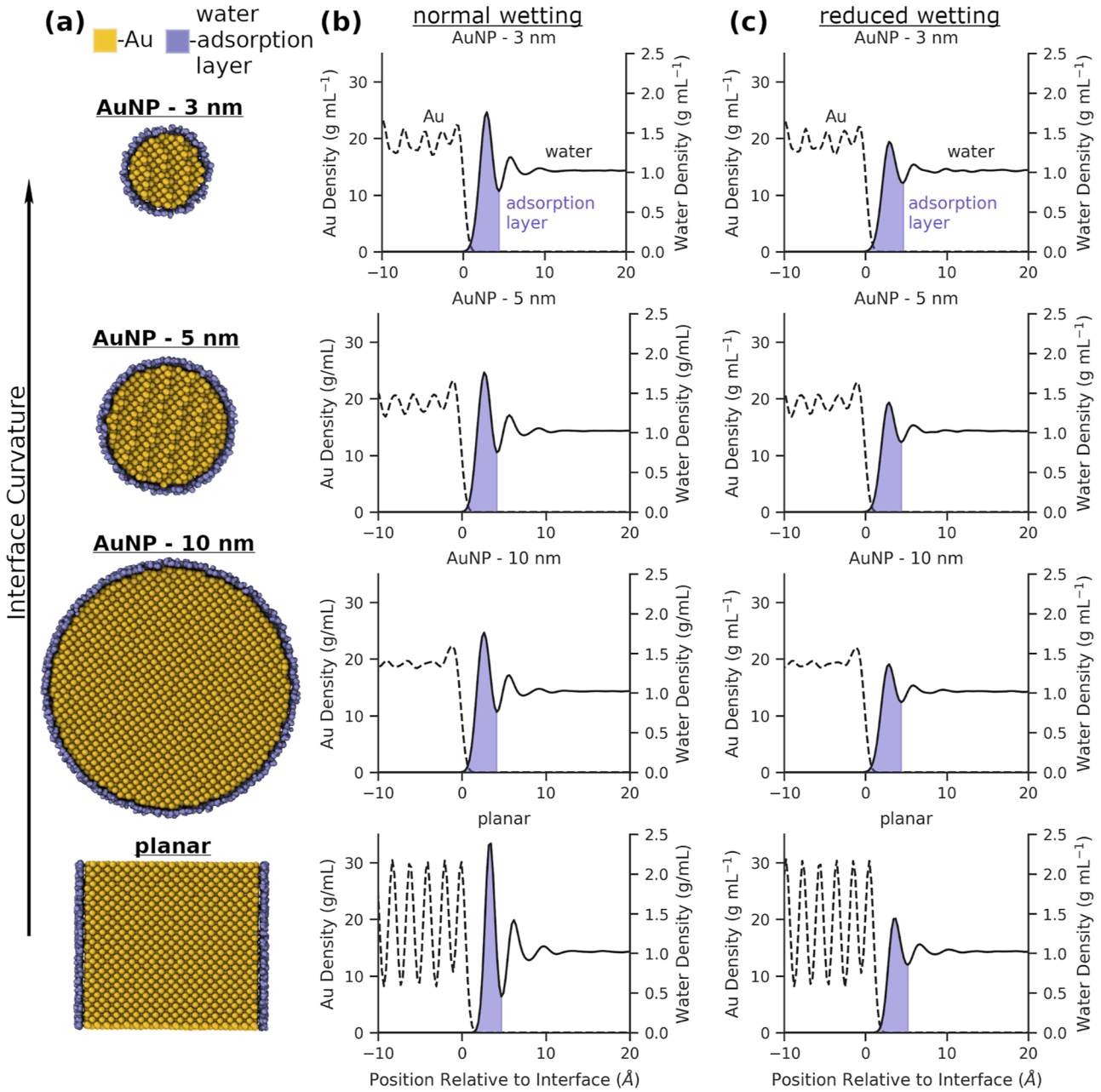

FIG. 5. Water adsorption at the surface of nanoscale gold. (a) Representative snapshot of a cross-section view of the AuNP–water interface (without heating, normal wetting) showing the first layer of water adsorbed onto the gold surface. (b) and (c) Mass density profiles of gold and water in the absence of heating (T = 300 K) for the moderate (b) and reduced wetting (c) cases; the layer of water adsorbed onto the gold surface is shaded in purple.

time averaged profiles were then further smoothed by applying a Gaussian filter with $\sigma = 2$ to generate the final equilibrium or steady-state profile. The surface adsorption density (ρ) for spherical AuNPs and the planar gold surface, respectively, was computed according to the following equations adapted from Tascini *et al.*:[27]

$$\rho = \frac{N_w}{A} = \frac{4N_A}{M_w d^2} \int_0^{r_{max}} r^2 \rho_w(r) dr, \tag{8}$$

$$\rho = \frac{N_w}{A} = \frac{N_A}{M_w} \int_0^{z_{max}} \rho_w(z) dz, \tag{9}$$

where N_w is the number of water molecules adsorbed on the surface of gold with surface area A, N_A is the Avogadro's number, M_w is the molar mass of water, $\rho_w(r)$ is the radial mass density of water at radius r, and $\rho_w(z)$ is the mass density of water along the direction perpendicular to the planar surface, z. The upper limits

of the integrals, r_{max} and z_{max}, were taken as the profile position corresponding to the minimum following the peak of the adsorption band [for example, see Figs. 5(b) and 5(c)]. The integrals were estimated using numerical quadrature.

For each wetting condition, we first examined the equilibrium density profiles of gold and water at 300 K (i.e., no heating) [Figs. 5(b) and 5(c)]. In the normal wetting case, the peak in the mass density corresponding to the adsorption layer was 1.7 g ml^{-1} for the AuNPs and 2.4 g ml^{-1} at the planar interface [Fig. 5(b)], whereas in the reduced wetting case, it was 1.4 g ml^{-1} for all the gold structures [Fig. 5(c)].

In the absence of heating, the surface adsorption density, ρ [Eqs. (8) and (9)], increased linearly with the gold–water interface curvature [Fig. 6(a)], regardless of the wetting strength. This result is consistent with the trends reported by Tascini *et al.* who observed an increase in surface adsorption density with interface curvature in simulations of spherical NPs immersed in a monatomic fluid at various wetting strengths.[27]

To better understand the curvature dependence of water adsorption at the gold surfaces, we examined how the relative solvent accessibility of the gold structures changed with interface curvature. Measures of solvent accessibility were developed in the context of proteins,[76,77] as a metric to help quantify the role of hydration in protein structure, folding and binding. We first computed the solvent-accessible surface area, A_{SASA}, of the initial configuration of each gold structure using the measure sasa function in VMD with a probe radius of 4.04 Å;[33] this probe radius corresponds to the minimum energy in the Lennard-Jones potential for the gold–water interaction in the normal wetting case. The following ratio quantified the relative accessibility: A_{SASA}/A, where A is the gold structure's surface area taken as $A = \pi d^2$ for spherical AuNPs and $A = 2L_xL_y$ for the planar slab. The relative accessibility A_{SASA}/A increased linearly with the interface curvature [Fig. 6(b)]. Since the solvent-accessible surface area, A_{SASA}, effectively quantifies the maximum amount of water that can adhere at the gold surfaces independent of wetting strength and temperature/heating, the trend in A_{SASA}/A suggests a geometric effect in which there is more space for water to adsorb at the curved gold surfaces. This is consistent with the recent analysis by Jiang *et al.* that indicates the coordination number of surface atoms in solid nanoparticles increases with particle size.[61] The more undercoordinated atoms at the surface of smaller particles thus allow greater solvent accessibility. This effect explains why the more highly curved gold surfaces sustain higher ρ in both the moderate and reduced wetting conditions.

We also analyzed the steady-state nonequilibrium molecular dynamics simulations and evaluated the steady-state density profiles of gold and water under each simulated heating power (Figs. S10 and S11, supplementary material). In most cases, there were only minor changes in the height and width of the peak corresponding to the water adsorption layer with heating. In the reduced wetting case, the distinct peak for the adsorption layer near the 5 and 10 nm AuNPs disappeared at heating powers of $Q = 4000$ nW and $Q = 8000$ nW, respectively (Fig. S11, supplementary material), exhibiting signs of temperature-induced desorption. However, we did not observe vapor nanobubble formation in any of the simulated cases, and the temperature of water at the interfaces was well below the experimental threshold for vapor nanobubble formation [Figs. S9(a) and S9(b), supplementary material].[11] Due to the reduction in interface

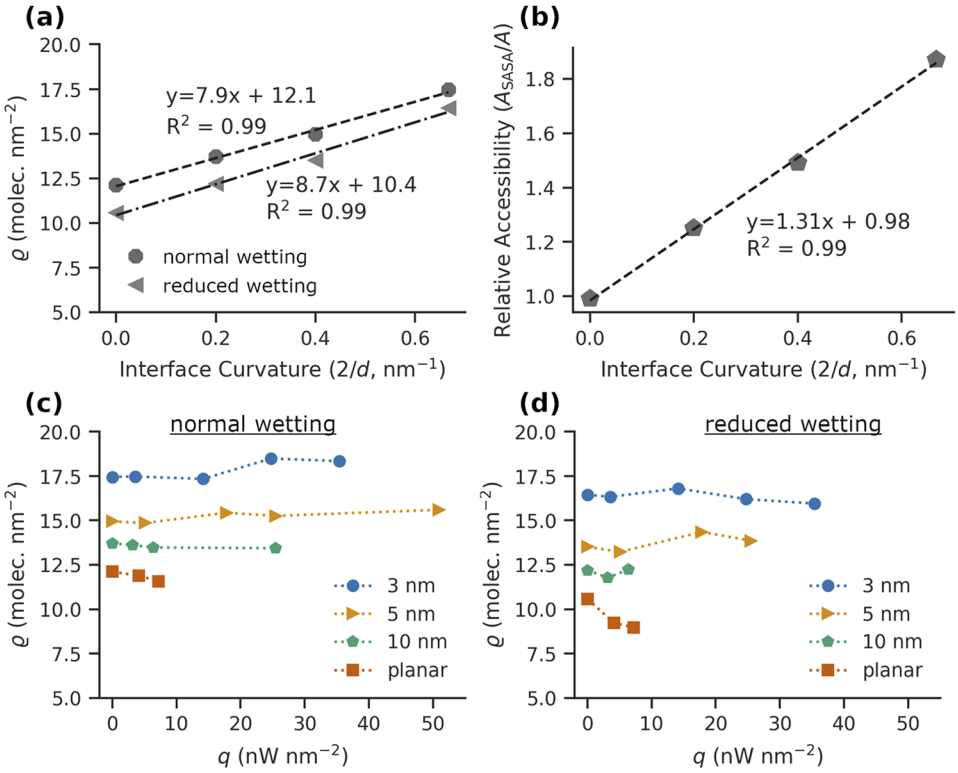

FIG. 6. Interface water adsorption increases with interface curvature but not applied heat flux. (a) Surface adsorption density of water vs interface curvature in the absence of heating for the moderate and reduced wetting cases; the dashed line shows the linear fit. (b) Relative accessibility (A_{SASA}/A) vs interface curvature. The dashed line shows the linear fit to the data. (c) and (d) Water adsorption density vs heat flux for the different gold–water interfaces under moderate (c) and poor (d) wetting conditions.

conductance, the gold structures under normal wetting have higher temperatures than in the normal wetting case [Figs. S9(c) and S9(d)], and through visual inspection of the simulation trajectories, the reduced wetting AuNPs were observed to be molten under some heating conditions. Putting aside the two cases that exhibited signs of temperature-induced desorption, under both wetting conditions the surface adsorption density ρ was relatively unaffected by heating and did not exhibit any clear dependence on heat flux [Figs. 6(c) and 6(d)]. This result suggests that the amount of water in the first adsorption layer remains relatively constant during heating, and it is consistent with the temperature-induced desorption being a threshold event that depends on both the water temperature and the gold wettability. Since there were only minor changes in the height and width of the peak corresponding to the water adsorption layer with heating power in the normal wetting case, and no consistent heat flux dependence in the surface adsorption density, we conclude that changes in the water density near the surface of the gold structures alone are not sufficient to explain the temperature dependence of G in the normal wetting case.

C. Analysis of nanoscale gold and water vibrational density of states

In the absence of electron–phonon coupling, interfacial heat transport is mediated by the transmission and scattering of phonons (vibrational energy carriers) across the interface.[18,78] In particular, models of thermal interface conductance based on diffuse mismatch emphasize coupling between the two materials' vibrational modes, or phonon density of states, as a critical factor in heat transport through the interface.[78,79] In molecular dynamics simulations, the vibrational coupling between nanomaterials and solvent can be qualitatively characterized by computing their respective vibrational density of states (VDOS) and comparing the overlap between the two distributions.[27,31,37,42] We estimated the VDOS of each gold structure and the surrounding water using a Fourier transform of the velocity autocorrelation function, as given by the following equation:

$$\mathrm{VDOS}(\omega) = \int_0^{+\infty} \langle \vec{v}(t) \cdot \vec{v}(0) \rangle \, e^{-i\omega t} \, dt, \tag{10}$$

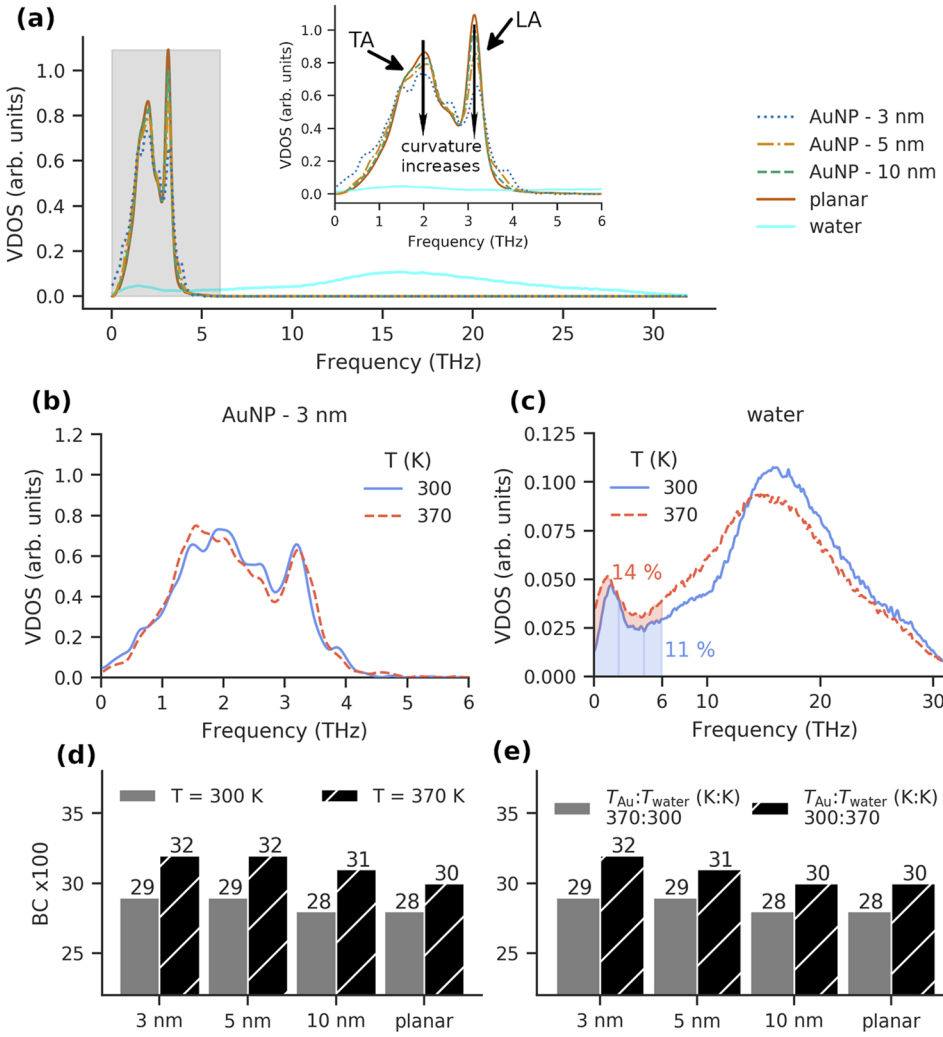

FIG. 7. Temperature-dependent shifts in water vibrational density of states (VDOS). (a) VDOS of gold and water at 300 K. The gray region denotes the frequency range 0–6 THz, which is shown in more detail in the inset. (b) VDOS of the 3 nm AuNP at 300 and 370 K. (c) Comparison of the water VDOS at 300 and 370 K. The shaded areas highlight the density in the range 0–6 THz with the labeled percentage by area. Note that in each case, when plotting the VDOS, we rescaled the density by the maximum value of the 10 nm AuNP so that y-axis ranges from 0 to ~1. (d) Comparison of the *BC* values for each gold surface computed from the VDOS at 300 and 370 K (gold and water are at the same temperature in each case). (e) Cross-temperature *BC* values for the two combinations of gold and water at different temperature (300 or 370 K).

where ω is the vibrational frequency and $\langle \vec{v}(t) \cdot \vec{v}(0) \rangle$ is the velocity autocorrelation function computed at a given temperature and averaged over all atoms of given type (either gold or water) and over multiple time origins (denoted by angular brackets); additional simulation details can be found in Sec. II B. First, we computed the VDOS of gold and water at 300 K [Fig. 7(a)]. The water distribution was broad, exhibiting a low intensity peak in the low frequency domain and a broad peak at higher frequency, consistent with previous reports.[30,42] Only the low frequency water peak has significant overlap with the VDOS of gold. The VDOS of gold was concentrated in the low frequency regime with two distinct peaks similar to the transverse (TA) and longitudinal (LA) acoustic modes in bulk gold,[80] consistent with previous reports [Fig. 7(a)].[42,81] Increasing the interface curvature leads to lower peak intensity and broader outer tails in the gold VDOS, especially for the LA mode [Fig. 7(a), inset]. Since the temperature of gold and nearby water are elevated (above 300 K) during heating (Fig. S9, supplementary material), we also computed the VDOS at 370 K and compared the results to those at 300 K [Figs. 7(b), 7(c), and S12, supplementary material]. The 3 nm AuNP exhibited the most obvious shift in VDOS [Fig. 7(b)], but overall the temperature-dependent changes in the gold VDOS were minor [Figs. 7(b) and S12, supplementary material]. In contrast, the water density underwent a noticeable redistribution to the lower frequency regime at 370 K [Fig. 7(c)]. The percentage of the water VDOS in the range 0–6 THz increased from 11% at 300 K to 14% at 370 K, which suggests there may be better vibrational coupling between gold and water at elevated water temperatures. Therefore, temperature-dependent shifts in the water VDOS may contribute to the increases in G with heat flux observed in the normal wetting case.

To further characterize the level of overlap between the gold and water VDOS, we estimated the Bhattacharyya coefficient (BC) between the gold and water VDOS,[82]

$$BC = \int \sqrt{\mathrm{VDOS}_{\mathrm{Au}}(\omega) \times \mathrm{VDOS}_{\mathrm{Water}}(\omega)}\, d\omega, \tag{11}$$

where ω is the vibrational frequency and $\mathrm{VDOS}_{\mathrm{Au}}(\omega)$ and $\mathrm{VDOS}_{\mathrm{Water}}(\omega)$ are the vibrational density of states (VDOS) of gold and water, respectively. The BC integral was numerically estimated for the range of frequencies 0–32 THz. The BC is a measure of overlap between probability distributions that ranges from 0 (no overlap) to 1 (perfect overlap). We computed the BC values for each gold structure–water VDOS combination at temperatures 300 and 370 K [Fig. 7(d)]. At 300 K, the BC values ranged from 0.28 to 0.29. At 370 K, the BC values increased to 0.30–0.32 [Fig. 7(d)], indicating improved overlap between the gold and water VDOS. To further confirm this effect, we computed the cross-temperature BC values [Fig. 7(e)]. Similarly, the BC only increased when the water temperature was 370 K, confirming that shifts in the water VDOS are the primary factor improving the overlap between the gold and water VDOS.

IV. CONCLUSIONS

In this work, we used atomistic molecular dynamics simulations to investigate the heat transfer through nanoscale gold–water interfaces. We simulated four nanoscale gold surfaces with differing curvatures, subjected to various heating intensities. We also simulated a hypothetical case in which the gold surface exhibited reduced wetting to evaluate whether such a change affected trends in the interface conductance with curvature or heating intensity. An analysis of the critical value of the thermal interface conductance confirmed that the thermal interface conductance is an important factor in the aqueous heat transfer of particles in the size range we investigated. We found that for a given AuNP size, the thermal interface conductance increased nonlinearly with the applied heat flux under normal wetting of the gold surface, and did not change under reduced wetting conditions. Analysis of the gold and water vibrational density of states showed a temperature-dependent shift in the water distribution that improved the overlap with the gold density of states. This shift in the water VDOS may contribute to the increases in thermal interface conductance with applied heat flux under the normal wetting condition. Our results also showed that the thermal interface conductance between nanoscale gold and water increased linearly with interface curvature at both low and high heat flux under both wetting conditions. Our analysis indicated that the curvature dependence of the interface conductance coincided with a curvature-dependent increase in water adsorption at the gold surfaces, consistent with that observed previously with a simpler model of solid nanospheres immersed in monatomic fluid.[27]

This work helps elucidate the temperature and curvature effects on the thermal conductance across nanoscale gold–water interfaces. However, our work here focused only on bare spherical particles immersed in water. Ligand functionalization can further alter the interfacial heat transport properties,[30,83,84] and for example, the effective thermal interface conductance may be modulated by ligand hydrophilicity.[25,75] Although we considered two conditions for the gold wettability, the heat transfer of bare AuNPs does not capture the added complexity introduced with ligand functionalization of gold. We also did not directly investigate how the observed temperature- and curvature-dependent changes in the thermal interface conductance impact the spatiotemporal temperature dynamics during pulsed laser stimulation of AuNPs, or how they might affect any particular application of photothermally heated AuNPs. Future work will be required to address these issues, as well as to experimentally validate our findings.

SUPPLEMENTARY MATERIAL

See the supplementary material for Tables S1–S4 and Figs. S1–S12. The following reference is cited in the supplementary material but not the main text.[85]

ACKNOWLEDGMENTS

The authors thank Dr. Hejian Xiong, Dr. Haihang Ye, Dr. Qi Cai, and Chen Xie for critically reading the manuscript and providing their feedback. The authors also acknowledge the Texas Advanced Computing Center (TACC) at The University of Texas at Austin for providing HPC resources that have contributed to these research results (URL: http://www.tacc.utexas.edu). Research reported in this work was supported by the National Institutes of Health under Award No. R35GM133653.

AUTHOR DECLARATIONS

Conflict of Interest

The authors have no conflicts to disclose.

Author Contributions

Blake A. Wilson: Conceptualization (supporting); Data curation (lead); Formal analysis (lead); Investigation (lead); Methodology (lead); Software (lead); Visualization (lead); Writing – original draft (lead); Writing – review & editing (equal). **Steven O. Nielsen:** Conceptualization (supporting); Methodology (supporting); Software (supporting); Visualization (supporting); Writing – original draft (supporting); Writing – review & editing (equal). **Jaona H. Randrianalisoa:** Conceptualization (supporting); Methodology (supporting); Visualization (supporting); Writing – original draft (supporting); Writing – review & editing (equal). **Zhenpeng Qin:** Conceptualization (lead); Funding acquisition (lead); Methodology (supporting); Supervision (lead); Visualization (supporting); Writing – original draft (supporting); Writing – review & editing (equal).

DATA AVAILABILITY

The data that support the findings of this study are available from the corresponding author upon reasonable request.

REFERENCES

[1] G. Baffou and R. Quidant, "Thermo-plasmonics: Using metallic nanostructures as nano-sources of heat," Laser Photonics Rev. **7**, 171–187 (2013).
[2] Z. Qin and J. C. Bischof, "Thermophysical and biological responses of gold nanoparticle laser heating," Chem. Soc. Rev. **41**, 1191–1217 (2012).
[3] G. Baffou, F. Cichos, and R. Quidant, "Applications and challenges of thermoplasmonics," Nat. Mater. **19**, 946–958 (2020).
[4] L. R. Hirsch, R. J. Stafford, J. A. Bankson, S. R. Sershen, B. Rivera, R. E. Price, J. D. Hazle, N. J. Halas, and J. L. West, "Nanoshell-mediated near-infrared thermal therapy of tumors under magnetic resonance guidance," Proc. Natl. Acad. Sci. U. S. A. **100**, 13549–13554 (2003).
[5] G. S. Terentyuk, G. N. Maslyakova, L. V. Suleymanova, N. G. Khlebtsov, B. N. Khlebtsov, G. G. Akchurin, I. L. Maksimova, and V. V. Tuchin, "Laser-induced tissue hyperthermia mediated by gold nanoparticles: Toward cancer phototherapy," J. Biomed. Opt. **14**, 021016 (2009).
[6] G. Huettmann, J. Serbin, B. Radt, B. I. Lange, and R. Birngruber, "Model system for investigating laser-induced subcellular microeffects," Proc. SPIE **4257**, 398 (2001).
[7] G. Huettmann, B. Radt, J. Serbin, and R. Birngruber, "Inactivation of proteins by irradiation of gold nanoparticles with nano- and picosecond laser pulses," Proc. SPIE **5142**, 88 (2003).
[8] C. M. Pitsillides, E. K. Joe, X. Wei, R. R. Anderson, and C. P. Lin, "Selective cell targeting with light-absorbing microparticles and nanoparticles," Biophys. J. **84**, 4023–4032 (2003).
[9] P. Kang, Z. Chen, S. O. Nielsen, K. Hoyt, S. D'Arcy, J. J. Gassensmith, and Z. Qin, "Molecular hyperthermia: Spatiotemporal protein unfolding and inactivation by nanosecond plasmonic heating," Small **13**, 1700841 (2017).
[10] P. Kang, X. Li, Y. Liu, S. I. Shiers, H. Xiong, M. Giannotta, E. Dejana, T. J. Price, J. Randrianalisoa, S. O. Nielsen, and Z. Qin, "Transient photoinactivation of cell membrane protein activity without genetic modification by molecular hyperthermia," ACS Nano **13**, 12487–12499 (2019).
[11] K. Metwally, S. Mensah, and G. Baffou, "Fluence threshold for photothermal bubble generation using plasmonic nanoparticles," J. Phys. Chem. C **119**, 28586–28596 (2015).
[12] A. Carattino, M. Caldarola, and M. Orrit, "Gold nanoparticles as absolute nanothermometers," Nano Lett. **18**, 874–880 (2018).
[13] D. A. Hastman, J. S. Melinger, G. L. Aragonés, P. D. Cunningham, M. Chiriboga, Z. J. Salvato, T. M. Salvato, C. W. Brown III, D. Mathur, I. L. Medintz, E. Oh, and S. A. Díaz, "Femtosecond laser pulse excitation of DNA-labeled gold nanoparticles: Establishing a quantitative local nanothermometer for biological applications," ACS Nano **14**, 8570–8583 (2020).
[14] D. Boyer, P. Tamarat, A. Maali, B. Lounis, and M. Orrit, "Photothermal imaging of nanometer-sized metal particles among scatterers," Science **297**, 1160–1163 (2002).
[15] M. Selmke, M. Braun, and F. Cichos, "Photothermal single-particle microscopy: Detection of a nanolens," ACS Nano **6**, 2741–2749 (2012).
[16] Y.-S. Chen, W. Frey, S. Kim, P. Kruizinga, K. Homan, and S. Emelianov, "Silica-coated gold nanorods as photoacoustic signal nanoamplifiers," Nano Lett. **11**, 348–354 (2011).
[17] X. Liu, M. G. González, R. Niessner, and C. Haisch, "Strong size-dependent photoacoustic effect on gold nanoparticles: A sensitive tool for aggregation-based colorimetric protein detection," Anal. Methods **4**, 309–311 (2012).
[18] D. G. Cahill, W. K. Ford, K. E. Goodson, G. D. Mahan, A. Majumdar, H. J. Maris, R. Merlin, and S. R. Phillpot, "Nanoscale thermal transport," J. Appl. Phys. **93**, 793–818 (2003).
[19] T. Luo and G. Chen, "Nanoscale heat transfer-from computation to experiment," Phys. Chem. Chem. Phys. **15**, 3389–3412 (2013).
[20] O. M. Wilson, X. Hu, D. G. Cahill, and P. V. Braun, "Colloidal metal particles as probes of nanoscale thermal transport in fluids," Phys. Rev. B **66**, 224301 (2002).
[21] A. Plech, V. Kotaidis, S. Grésillon, C. Dahmen, and G. von Plessen, "Laser-induced heating and melting of gold nanoparticles studied by time-resolved x-ray scattering," Phys. Rev. B **70**, 195423 (2004).
[22] Z. Ge, D. G. Cahill, and P. V. Braun, "AuPd metal nanoparticles as probes of nanoscale thermal transport in aqueous solution," J. Phys. Chem. B **108**, 18870–18875 (2004).
[23] Z. Ge, D. G. Cahill, and P. V. Braun, "Thermal conductance of hydrophilic and hydrophobic interfaces," Phys. Rev. Lett. **96**, 186101 (2006).
[24] A. J. Schmidt, J. D. Alper, M. Chiesa, G. Chen, S. K. Das, and K. Hamad-Schifferli, "Probing the gold nanorod–ligand–solvent interface by plasmonic absorption and thermal decay," J. Phys. Chem. C **112**, 13320–13323 (2008).
[25] J. Alper and K. Hamad-Schifferli, "Effect of ligands on thermal dissipation from gold nanorods," Langmuir **26**, 3786–3789 (2010).
[26] T. Stoll, P. Maioli, A. Crut, S. Rodal-Cedeira, I. Pastoriza-Santos, F. Vallée, and N. Del Fatti, "Time-resolved investigations of the cooling dynamics of metal nanoparticles: Impact of environment," J. Phys. Chem. C **119**, 12757–12764 (2015).
[27] A. S. Tascini, J. Armstrong, E. Chiavazzo, M. Fasano, P. Asinari, and F. Bresme, "Thermal transport across nanoparticle–fluid interfaces: The interplay of interfacial curvature and nanoparticle–fluid interactions," Phys. Chem. Chem. Phys. **19**, 3244–3253 (2017).
[28] A. R. Nair and S. P. Sathian, "Heat transfer across nanoparticle–liquid interfaces," J. Heat Transfer **138**, 112402 (2016).
[29] A. Lervik, F. Bresme, and S. Kjelstrup, "Heat transfer in soft nanoscale interfaces: The influence of interface curvature," Soft Matter **5**, 2407–2414 (2009).
[30] K. M. Stocker, S. M. Neidhart, and J. D. Gezelter, "Interfacial thermal conductance of thiolate-protected gold nanospheres," J. Appl. Phys. **119**, 025106 (2016).
[31] S. M. Neidhart and J. D. Gezelter, "Thermal transport is influenced by nanoparticle morphology: A molecular dynamics study," J. Phys. Chem. C **122**, 1430–1436 (2018).
[32] M. Hu and G. V. Hartland, "Heat dissipation for Au particles in aqueous solution: Relaxation time versus size," J. Phys. Chem. B **106**, 7029–7033 (2002).
[33] W. Humphrey, A. Dalke, and K. Schulten, "VMD: Visual molecular dynamics," J. Mol. Graphics **14**, 33–38 (1996).
[34] S. Plimpton, "Fast parallel algorithms for short-range molecular dynamics," J. Comput. Phys. **117**, 1–19 (1995).

[35]S. M. Foiles, M. I. Baskes, and M. S. Daw, "Embedded-atom-method functions for the fcc metals Cu, Ag, Au, Ni, Pd, Pt, and their alloys," Phys. Rev. B **33**, 7983–7991 (1986).
[36]J. López-Lemus, G. A. Chapela, and J. Alejandre, "Effect of flexibility on surface tension and coexisting densities of water," J. Chem. Phys. **128**, 174703 (2008).
[37]S. Merabia, S. Shenogin, L. Joly, P. Keblinski, and J.-L. Barrat, "Heat transfer from nanoparticles: A corresponding state analysis," Proc. Natl. Acad. Sci. U. S. A. **106**, 15113 (2009).
[38]Y. Dou, L. V. Zhigilei, N. Winograd, and B. J. Garrison, "Explosive boiling of water films adjacent to heated surfaces: A microscopic description," J. Phys. Chem. A **105**, 2748–2755 (2001).
[39]P. Schravendijk, N. van der Vegt, L. Delle Site, and K. Kremer, "Dual-scale modeling of benzene adsorption onto Ni(111) and Au(111) surfaces in explicit water," ChemPhysChem **6**, 1866–1871 (2005).
[40]K. A. Tay and F. Bresme, "Wetting properties of passivated metal nanocrystals at liquid–vapor interfaces: A computer simulation study," J. Am. Chem. Soc. **128**, 14166–14175 (2006).
[41]A. V. Verde, J. M. Acres, and J. K. Maranas, "Investigating the specificity of peptide adsorption on gold using molecular dynamics simulations," Biomacromolecules **10**, 2118–2128 (2009).
[42]X. Chen, A. Munjiza, K. Zhang, and D. Wen, "Molecular dynamics simulation of heat transfer from a gold nanoparticle to a water pool," J. Phys. Chem. C **118**, 1285–1293 (2014).
[43]F. Iori and S. Corni, "Including image charge effects in the molecular dynamics simulations of molecules on metal surfaces," J. Comput. Chem. **29**, 1656–1666 (2008).
[44]F. Iori, R. Di Felice, E. Molinari, and S. Corni, "GolP: An atomistic force-field to describe the interaction of proteins with Au(111) surfaces in water," J. Comput. Chem. **30**, 1465–1476 (2008).
[45]H. Bhattarai, K. E. Newman, and J. D. Gezelter, "The role of polarizability in the interfacial thermal conductance at the gold–water interface," J. Chem. Phys. **153**, 204703 (2020).
[46]Y. Wang and P. Keblinski, "Role of wetting and nanoscale roughness on thermal conductance at liquid-solid interface," Appl. Phys. Lett. **99**, 073112 (2011).
[47]R. Hockney and J. Eastwood, "The particle-mesh force calculation," in *Computer Simulation Using Particles* (CRC Press, 1989), pp. 120–165.
[48]T. Schneider and E. Stoll, "Molecular-dynamics study of a three-dimensional one-component model for distortive phase transitions," Phys. Rev. B **17**, 1302 (1978).
[49]N. Michaud-Agrawal, E. J. Denning, T. B. Woolf, and O. Beckstein, "MDAnalysis: A toolkit for the analysis of molecular dynamics simulations," J. Comput. Chem. **32**, 2319–2327 (2011).
[50]R. J. Gowers, M. Linke, J. Barnoud, T. J. E. Reddy, M. N. Melo, S. L. Seyler, J. Domański, D. L. Dotson, S. Buchoux, I. M. Kenney, and O. Beckstein, "MDAnalysis: A Python package for the rapid analysis of molecular dynamics simulations," in *Proceedings of the 15th Python in Science Conference*, edited by S. Benthall and S. Rostrup (SciPy, 2016), pp. 98–105.
[51]P. Virtanen, R. Gommers, T. E. Oliphant, M. Haberland, T. Reddy, D. Cournapeau, E. Burovski, P. Peterson, W. Weckesser, J. Bright, S. J. van der Walt, M. Brett, J. Wilson, K. J. Millman, N. Mayorov, A. R. J. Nelson, E. Jones, R. Kern, E. Larson, C. J. Carey, İ. Polat, Y. Feng, E. W. Moore, J. VanderPlas, D. Laxalde, J. Perktold, R. Cimrman, I. Henriksen, E. A. Quintero, C. R. Harris, A. M. Archibald, A. H. Ribeiro, F. Pedregosa, P. van Mulbregt, and SciPy 1.0 Contributors, "SciPy 1.0: Fundamental algorithms for scientific computing in Python," Nat. Methods **17**, 261–272 (2020).
[52]C. R. Harris, K. J. Millman, S. J. van der Walt, R. Gommers, P. Virtanen, D. Cournapeau, E. Wieser, J. Taylor, S. Berg, N. J. Smith, R. Kern, M. Picus, S. Hoyer, M. H. van Kerkwijk, M. Brett, A. Haldane, J. F. del Río, M. Wiebe, P. Peterson, P. Gérard-Marchant, K. Sheppard, T. Reddy, W. Weckesser, H. Abbasi, C. Gohlke, and T. E. Oliphant, "Array programming with NumPy," Nature **585**, 357–362 (2020).
[53]J. D. Hunter, "Matplotlib: A 2D graphics environment," Comput. Sci. Eng. **9**, 90–95 (2007).
[54]M. L. Waskom, "seaborn: Statistical data visualization," J. Open Source Software **6**, 3021 (2021).
[55]S. K. Lam, A. Pitrou, and S. Seibert, "Numba: A LLVM-based Python JIT compiler," in *Proceedings of the Second Workshop on the LLVM Compiler Infrastructure in HPC, LLVM '15* (Association for Computing Machinery, New York, 2015).
[56]W. McKinney, "Data structures for statistical computing in Python," in *Proceedings of the 9th Python in Science Conference* (SciPy, 2010), pp. 56–61.
[57]T. Kluyver, B. Ragan-Kelley, F. Pérez, B. Granger, M. Bussonnier, J. Frederic, K. Kelley, J. Hamrick, J. Grout, S. Corlay, P. Ivanov, D. Avila, S. Abdalla, and C. Willing, "Jupyter notebooks—A publishing format for reproducible computational workflows," in *Positioning and Power in Academic Publishing: Players, Agents and Agendas*, edited by F. Loizides and B. Schmidt (IOS Press, 2016), pp. 87–90.
[58]J. Stone, "An efficient library for parallel ray tracing and animation," M.S. thesis, Computer Science Department, University of Missouri-Rolla, 1998.
[59]A. Grossfield and D. M. Zuckerman, "Quantifying uncertainty and sampling quality in biomolecular simulations," Annu. Rep. Comput. Chem. **5**, 23–48 (2009).
[60]J. D. Olarte-Plata, J. Gabriel, P. Albella, and F. Bresme, "Spatial control of heat flow at the nanoscale using Janus particles," ACS Nano **16**, 694–709 (2022).
[61]M. Jiang, J. D. Olarte-Plata, and F. Bresme, "Heterogeneous thermal conductance of nanoparticle–fluid interfaces: An atomistic nodal approach," J. Chem. Phys. **156**, 044701 (2022).
[62]C.-W. Nan, R. Birringer, D. R. Clarke, and H. Gleiter, "Effective thermal conductivity of particulate composites with interfacial thermal resistance," J. Appl. Phys. **81**, 6692–6699 (1997).
[63]C.-W. Nan and R. Birringer, "Determining the Kapitza resistance and the thermal conductivity of polycrystals: A simple model," Phys. Rev. B **57**, 8264–8268 (1998).
[64]M. L. V. Ramires, C. A. Nieto de Castro, Y. Nagasaka, A. Nagashima, M. J. Assael, and W. A. Wakeham, "Standard reference data for the thermal conductivity of water," J. Phys. Chem. Ref. Data **24**, 1377–1381 (1995).
[65]A. Plech, S. Ibrahimkutty, S. Reich, and G. Newby, "Thermal dynamics of pulsed-laser excited gold nanorods in suspension," Nanoscale **9**, 17284–17292 (2017).
[66]H.-K. Lyeo and D. G. Cahill, "Thermal conductance of interfaces between highly dissimilar materials," Phys. Rev. B **73**, 144301 (2006).
[67]P. E. Hopkins, P. M. Norris, and R. J. Stevens, "Influence of inelastic scattering at metal-dielectric interfaces," J. Heat Transfer **130**, 022401 (2008).
[68]S. Murad and I. K. Puri, "Thermal transport across nanoscale solid-fluid interfaces," Appl. Phys. Lett. **92**, 133105 (2008).
[69]S. Murad and I. K. Puri, "Molecular simulation of thermal transport across hydrophilic interfaces," Chem. Phys. Lett. **467**, 110–113 (2008).
[70]G. Balasubramanian, S. Banerjee, and I. K. Puri, "Unsteady nanoscale thermal transport across a solid-fluid interface," J. Appl. Phys. **104**, 064306 (2008).
[71]B. H. Kim, A. Beskok, and T. Cagin, "Molecular dynamics simulations of thermal resistance at the liquid-solid interface," J. Chem. Phys. **129**, 174701 (2008).
[72]Z. Shi, M. Barisik, and A. Beskok, "Molecular dynamics modeling of thermal resistance at argon-graphite and argon-silver interfaces," Int. J. Therm. Sci. **59**, 29–37 (2012).
[73]M. Hu, D. Poulikakos, C. P. Grigoropoulos, and H. Pan, "Recrystallization of picosecond laser-melted ZnO nanoparticles in a liquid: A molecular dynamics study," J. Chem. Phys. **132**, 164504 (2010).
[74]N. Shenogina, R. Godawat, P. Keblinski, and S. Garde, "How wetting and adhesion affect thermal conductance of a range of hydrophobic to hydrophilic aqueous interfaces," Phys. Rev. Lett. **102**, 156101 (2009).
[75]S.-W. Hung, G. Kikugawa, and J. Shiomi, "Mechanism of temperature dependent thermal transport across the interface between self-assembled monolayer and water," J. Phys. Chem. C **120**, 26678–26685 (2016).
[76]B. Lee and F. M. Richards, "The interpretation of protein structures: Estimation of static accessibility," J. Mol. Biol. **55**, 379–400 (1971).
[77]A. Shrake and J. A. Rupley, "Environment and exposure to solvent of protein atoms. Lysozyme and insulin," J. Mol. Biol. **79**, 351–371 (1973).

[78]E. T. Swartz and R. O. Pohl, "Thermal boundary resistance," Rev. Mod. Phys. **61**, 605–668 (1989).
[79]P. Reddy, K. Castelino, and A. Majumdar, "Diffuse mismatch model of thermal boundary conductance using exact phonon dispersion," Appl. Phys. Lett. **87**, 211908 (2005).
[80]J. W. Lynn, H. G. Smith, and R. M. Nicklow, "Lattice dynamics of gold," Phys. Rev. B **8**, 3493–3499 (1973).
[81]R. Carles, P. Benzo, B. Pécassou, and C. Bonafos, "Vibrational density of states and thermodynamics at the nanoscale: The 3D-2D transition in gold nanostructures," Sci. Rep. **6**, 39164 (2016).
[82]A. Bhattacharya, "On a measure of divergence between two multinomial populations," Indian J. Stat. **7**, 401–406 (1946).
[83]K. M. Stocker and J. D. Gezelter, "Simulations of heat conduction at thiolate-capped gold surfaces: The role of chain length and solvent penetration," J. Phys. Chem. C **117**, 7605–7612 (2013).
[84]S. Salassi, A. Cardellini, P. Asinari, R. Ferrando, and G. Rossi, "Water dynamics affects thermal transport at the surface of hydrophobic and hydrophilic irradiated nanoparticles," Nanoscale Adv. **2**, 3181–3190 (2020).
[85]F. Font and T. G. Myers, "Spherically symmetric nanoparticle melting with a variable phase change temperature," J. Nanopart. Res. **15**, 2086 (2013).